Lithosphere

Research Article

Multistage Strike-Slip Fault in the Narrowest Portion of the Qinling Orogen, Central China: Deformation Mechanism and Tectonic Significance

Yiping Zhang[1], **Xuanhua Chen**[1], **Yannan Wang**,[2] **Andrew V. Zuza**,[3] **Jin Zhang**,[4] **Bing Li**,[1] **Yongchao Wang**,[1] **Ye Wang**,[1] **Kui Liu**,[1] **Lele Han**,[1] **Beihang Zhang**,[4] **and Heng Zhao**[4]

[1]*Chinese Academy of Geological Sciences, Beijing, China*
[2]*Key Laboratory of Resource Exploration Research of Hebei Province, Hebei University of Engineering, Handan, China*
[3]*Nevada Bureau of Mines and Geology, University of Nevada, Reno, USA*
[4]*Institute of Geology, Chinese Academy of Geological Sciences, Beijing, China*

Correspondence should be addressed to Yiping Zhang; BJZhYP@126.com and Xuanhua Chen; xhchen@cags.ac.cn

The North Huicheng Basin strike-slip fault system is on the northeastern frontier of the Tibetan Plateau and separates the West and East Qinling differential orogeny. However, the deformation mechanism of this strike-slip fault system and its exact tectonic significance are unclear. Here, we carried out systematic field structural analysis, physical analog modeling, and multiproxy geochronological dating to address these issues. The field structural analysis indicates that the North Huicheng Basin strike-slip fault system was induced from the plate-like movement of the West and East Qinling Orogens, which underwent multiple left-lateral strike-slip faulting and controlled salient and recessed structures. The scaled physical analog experiment results confirm this hypothesis and reveal the primary spatial-temporal deformational kinematic process. Combined with published works, multiproxy geochronological dating (zircon U–Pb age of 213 Ma, biotite $^{40}Ar/^{39}Ar$ age of 203 Ma, and apatite fission-track age of 56 Ma) outlines the main thermal history of the hanging wall. Based on the above facts, the integrated research suggests that multistage strike-slip faulting played a significant role in the main tectonic events, that is, late Triassic magmatic emplacement, Jurassic/Cretaceous local pull-apart, and Cenozoic rapid exhumation driven by Tibetan Plateau growth.

1. Introduction

Strike-slip faults play an important role in continental deformation and have been observed widely in nature and analog experiments [1–6]. Strike-slip faults have been discussed in plate-like rigid-body motion models [1] and viscous flow models [3, 7]. Different end-member processes result in different strike-slip fault deformation kinematics, especially for the Altyn Tagh, Haiyuan, West Qinling, East Kunlun, Xianshuihe, and Ailao Shan-Red River faults (Figure 1(a)) [1, 5, 8–12]. In the northeastern Tibetan Plateau, the kinematics of these strike-slip faults have been summarized [5] in the lateral extrusion model [1, 13], transfer fault model [14, 15], rigid bookshelf fault model [16], and nonrigid bookshelf fault model [5]. The interaction between strike-slip fault systems and associated structures commonly involves different deformation mechanisms and continental dynamics [5, 9, 11, 12, 17, 18].

The E–W-trending Qinling Orogen defines a transitional zone between the Tibetan Plateau and the eastern lower-elevation continent (Figure 1), and it features well-developed strike-slip faults, such as the West Qinling, East Kunlun, and North Huicheng Basin faults [17–19] (Figure 1(b)), which facilitate the outgrowth of the Tibetan Plateau [20–25] and lateral extrusion of the Qinling Orogen [26]. The East Kunlun fault may have originally connected the Mianlue suture and marked the south boundary between the West Qinling Orogen and Songpan-Ganzi (Figure 1).
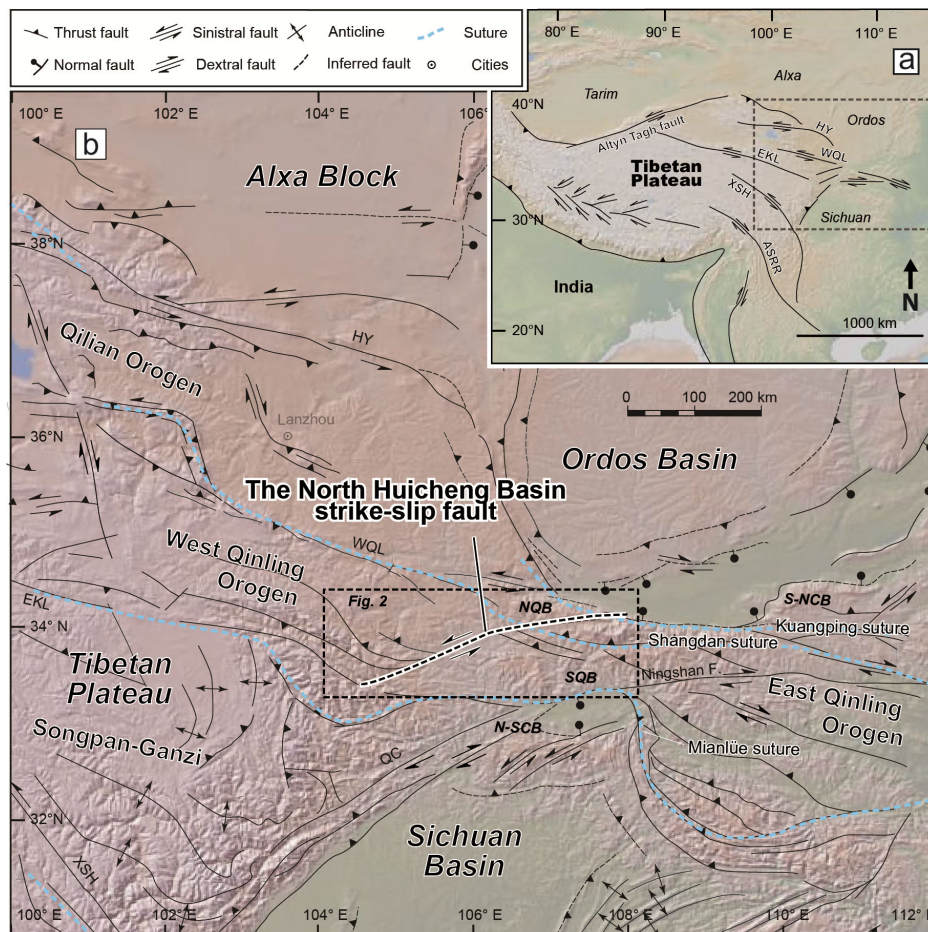
FIGURE 1: Sketch of the main structures in the Tibetan Plateau and Qinling Orogen region. (a) Strike-slip faults along the Tibetan Plateau margin. (b) Simplified structural sketch map of the northeastern Tibetan Plateau, where a strike-slip fault system has developed in the narrowest portion of the Qinling Orogen. HY—Haiyuan fault, WQL—West Qinling fault, EKL—East Kunlun fault, QC—Qingchuan fault, XSH—Xianshuihe fault, ASRR—Ailao Shan-Red River fault, S-NCB—Southern North China Block, NQB—North Qinling Orogenic Belt, SQB—South Qinling Orogenic Belt, and N-SCB—Northern South China Block. The digital topographic base maps are available at http://www.geomapapp.org/.

The West Qinling fault facilitated the Tibetan Plateau material transportation through left-lateral slipping. The North Huicheng Basin strike-slip fault system developed in the narrowest portion of the Qinling Orogen and acted as the structural boundary between the West and East Qinling Orogens [27–29] (Figures 1 and 2). Many studies have been performed, such as structural analysis [22, 30–36], geochronological dating [22, 36–39], magmatic emplacement [28], and sedimentary basin [40, 41]. Along this strike-slip fault system, prominent salient and recessed structures significantly affect crustal thickening, magmatic emplacement, and basin evolution (Figure 2). However, the deformation mechanisms of the strike-slip fault system and its tectonic significance are unclear, which impedes our comprehensive understanding of continental deformation and related tectonic events. The shortening style of the main strike-slip fault is a key factor in the spatial-temporal deformational kinematics (Figures 2 and 3). If shortening occurs in one direction (Figure 3(b)), the dip direction of the curved thrust faults should be consistent; otherwise, it is

the opposite if shortening occurs in two directions (Figure 3(a)).

In this study, we carried out a combination of fieldwork and physical analog modeling (with particle image velocimetry [PIV] mapping) on the North Huicheng Basin strike-slip fault system, which outlines the deformation mechanism of this strike-slip fault system and associated salient and recessed structures. Multiproxy geochronologic data were used to establish the main thermal history of the hanging wall. Integrated research suggests that this multistage strike-slip faulting plays a significant role in the main tectonic events.

2. Geologic Background

Previous studies have identified the main collisional events in the Qinling orogen, characterized by the Proterozoic Kuanping [42], Paleozoic Shangdan, and Triassic Mianlue sutures (Figure 1(b)) [31, 33, 42–44]. The main framework of the Qinling Orogen consists of the southern North China
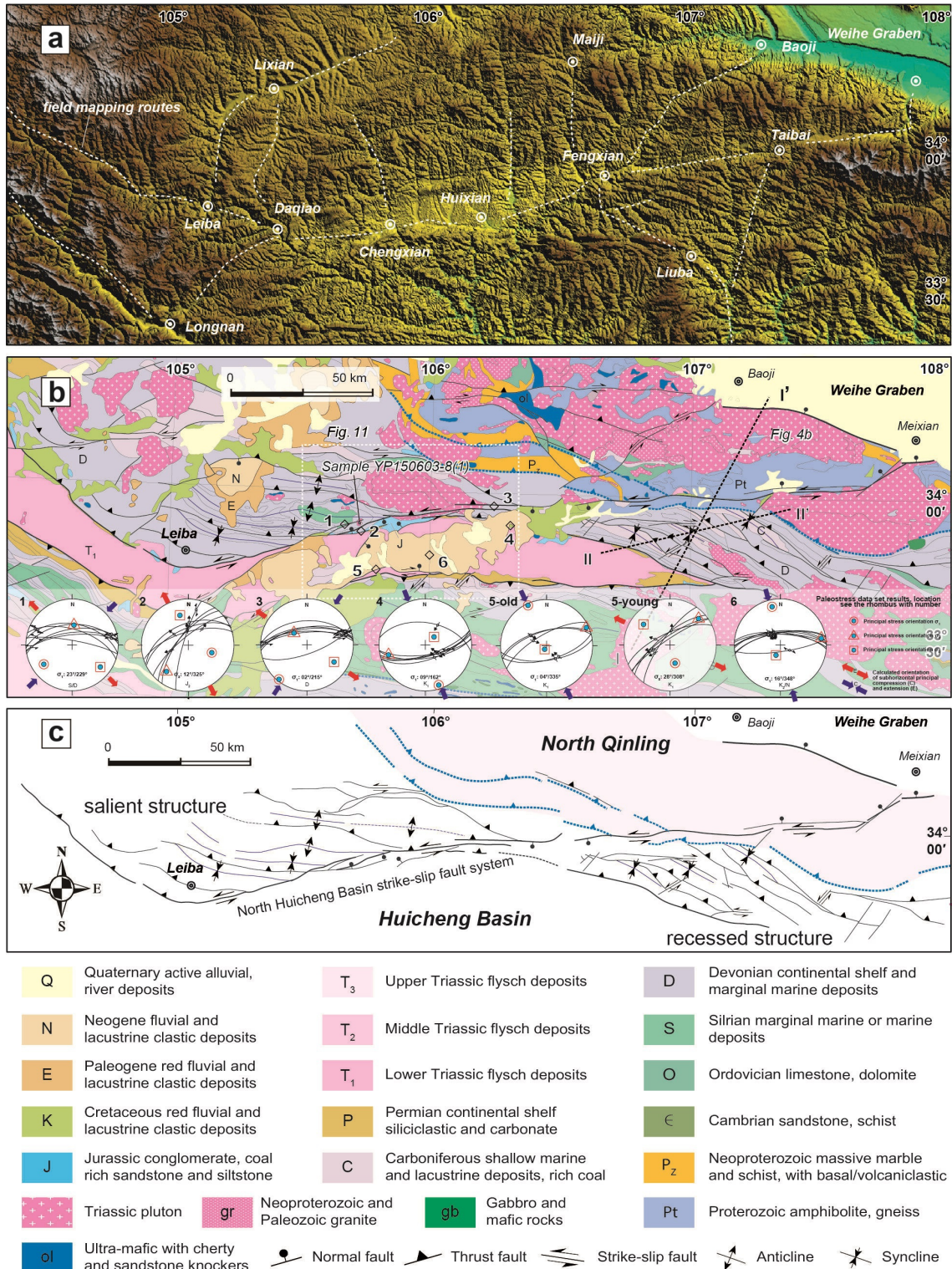
FIGURE 2: Field observations in the narrowest portion of the Qinling Orogen. (a) Field mapping routes (white dashed line) across the main region of structural trace based on the digital elevation model image. (b) Geologic map of the Qinling Orogen; the location is shown in Figure 1(b,c). Simplified structural system with salient structures to the west and recessed structures to the east. In addition, the calculated paleostress data sets and locations (diamond with a number) are labeled in Figure 2(b). Equal-area stereograms show fault-slip data and principal stress orientations (σ_1, σ_2, and σ_3; lower hemisphere). Faults are drawn as great circles, and striae are drawn as arrows pointing in the direction of the displacement of the hanging wall. The principal stress orientations were calculated via the PBT method (P = contraction-axis, B = neutral-axis, T = extension-axis.).. See Table 1 and the text for details.

(a) Two direction shortening model   **(b) One direction shortening model**
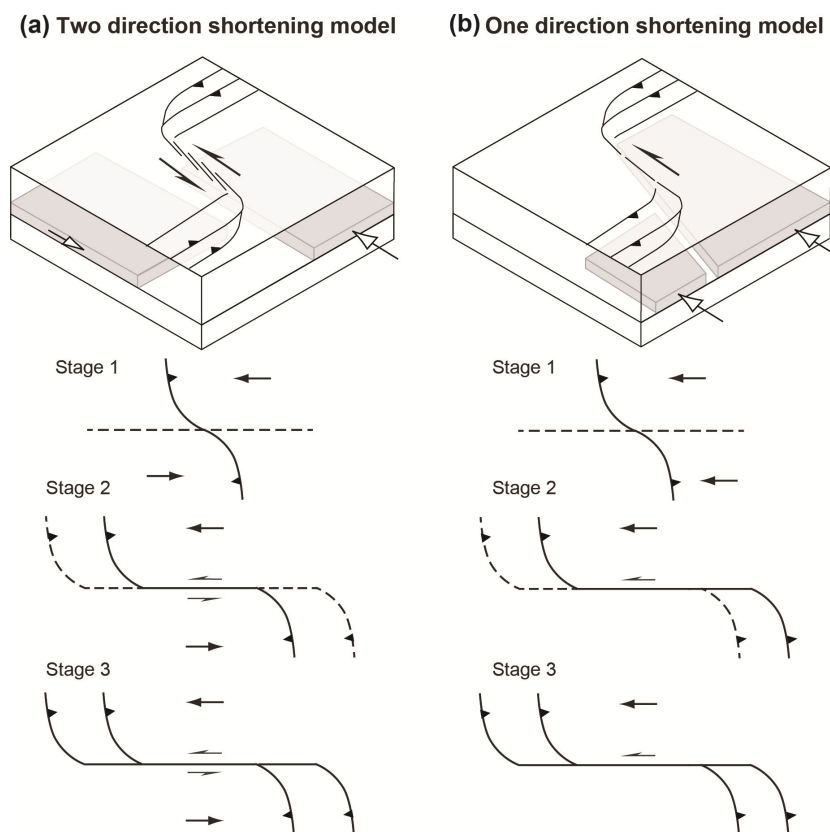

FIGURE 3: Different models of the deformation kinematics of the North Huicheng Basin strike-slip fault and associated structures. (a) Two-directional shortening model with oppositely dipping thrust faults, indicating two contractional stresses. (b) One-directional shortening model with consistently dipping thrust faults, indicating one contraction stress.

Block, North Qinling Belt, South Qinling Belt, and northern South China Block (Figure 1(b)) [31, 33]. Laterally, the Qinling Orogen was divided into the East and West Qinling Orogens with diverse topography and geology (Figure 1(b)). The East Qinling and West Qinling Orogens are connected with a narrow portion, which features a sharp decrease in width to 60–80 km and underwent greater crustal shortening [28, 36]. The structural boundary of the West and East Qinling Orogens is the NE-striking North Huicheng Basin fault system (Figure 1(b)) [27–29, 35], consisting of a series of substrike-slip faults (Figure 2).

The basement of the Qinling Orogen consists of Proterozoic amphibolite, quartzite, and quartz schist (Figures 2(b) and 4(a)) [42]. Silurian outcrops are present in South Qinling and predominantly consist of deep-marine siliciclastic rocks and turbidites [45]. Devonian marine sandstones and Carboniferous continental marginal deposits are also present (Figures 2(b), 4(a) and 5(d)) [46]. Permian to early Triassic siliciclastic and carbonate rocks were deposited in the Huicheng Basin (Figures 2(b), 4(a) and 5(f)). Middle Jurassic Longjiagou Formation lacustrine sandstone, shale, and interlayered coal occur occasionally in the northern Huicheng Basin (Figure 5(e)) [40]. Lower Cretaceous terrestrial conglomerate, sandstone, and other clastic rocks of the Donghe Group unconformably cover the older strata (Figure 5(a)–5(c)) [46]. Neogene–Holocene

rocks were deposited in the Huicheng Basin [46] (Figure 2(b)).

3. Structural and Geochronological Analysis

3.1. Methods. Systematic field transects across the main region of the main structural trace were constructed based on a digital elevation model (DEM) image (Figure 2(a)). With field observations, the fault-slip data are analyzed according to the kinematic approach of Marrett and Allmendinger [47] to assess incremental shortening or extension directions. P-B-T axes method is used to calculate the fault plane solutions and to visualize the structural data.

One hanging wall plutonic sample was collected for zircon U-Pb dating, biotite ^{40}Ar/^{39}Ar dating, and apatite fission-track (AFT) analyses. Different closure temperature results can be obtained from the same sample (zircon U-Pb >900°C [48]; biotite ^{40}Ar/^{39}Ar ~300 ± 50°C [49], ; and AFT 60°C–110°C [50]. Under this sampling strategy, the thermal history of the hanging wall can be approximately determined. The detailed geochronological analytical processes are listed in online supplementary material 1.

3.2. Results. Based on a compilation of published work [33, 36, 40], DEM images (Figure 2(a)), and field observations, we carried out a new interpretation of
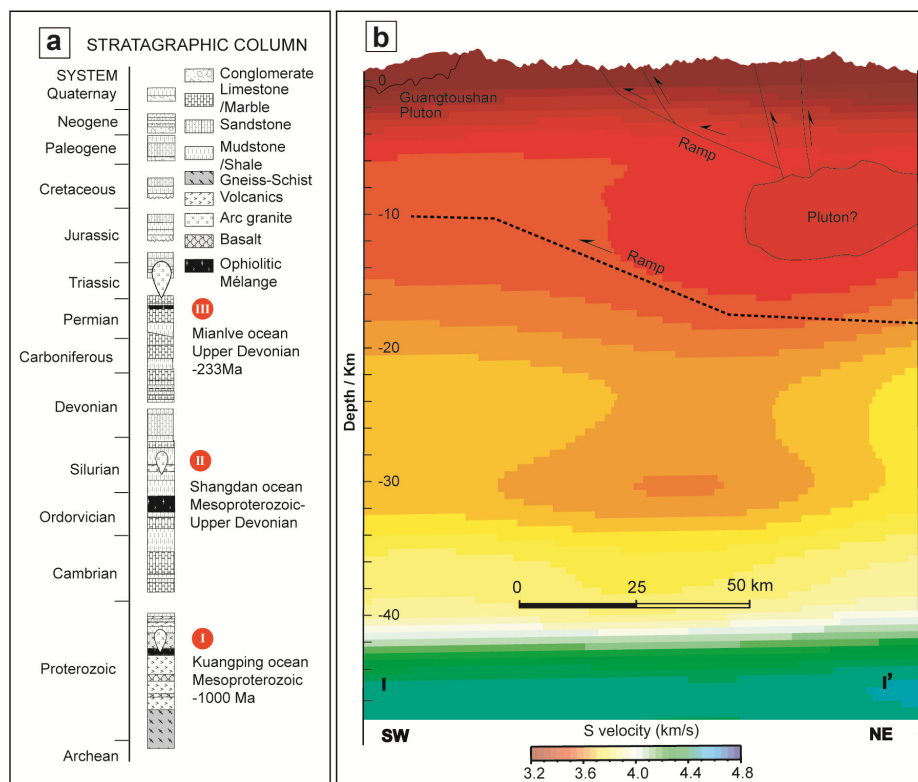
FIGURE 4: (a) Main stratigraphic column and typical sedimentary characteristics in the Qinling Orogen. (b) S-wave velocity profile and possible crustal-scale structures across the recessed structures to the east (profile I-I′ location shown in Figure 2(b), modified from Reference 36, horizontal and vertical scales are not consistent). In this image, some low-velocity anomalies are plotted in the mid-lower crust, and a detailed description is given in the text.

the structure of the North Huicheng Basin strike-slip fault system and neighboring region (Figure 2(b) and 2(c)). To the west, the Devonian to Carboniferous rocks form a highly deformed WNW–ESE-trending fold-and-thrust belt, forming salient structures. To the east, the NW–SE-trending fold-and-thrust belt is shortened into fault-related folds as recessed structures (Figure 2(c)). Seven sets of paleostress tensor data from different strata along the North Huicheng Basin fault (Table 1, Figure 2(b)) have been collected, which implies multiple complex tectonic events. Data sets 1 and 3 suggest principal stress orientations σ_1 of 229° and 215°; data set 2 suggests that the principal stress orientation σ_2 is at 325°; data sets 4, 5-old, and 6 suggest principal stress orientations σ_1 at 162°, 335°, and 348°; and data set 5-young suggests a σ_2 orientation of 308° (Table 1, Figure 2(b)).

Zircon U–Pb dating yields a concordant age of 213 ± 0.7 Ma (Figure 6(a)), which is obtained from 18 valid zircons after discordant correction. All the zircon Th/U ratios are larger than 0.1 (Table 2). For biotite $^{40}Ar/^{39}Ar$ dating, we exclude several initial and final stages of the sample because the Ar loss might be related to slight alteration and crystal structure damage. Thus, the $^{40}Ar/^{39}Ar$ ages yield a well-defined plateau age of 203.7 ± 1.8 Ma during the 980°C–1400°C phases (Figure 6(b); Table 3). For AFT dating, the granite sample yields a

pooled age of 56 ± 4 Ma for P (χ^2) > 5%, with a mean track length of 11.3 ± 2.4 μm (Figure 6(c); Table 4). The detailed AFT age, Dpar, and length data are listed in online supplementary Tables S1 and S2. In addition, combined with published works, we established the main thermal history of the hanging wall of the North Huicheng Basin fault system (Figure 6(d)). Combined with the paleostress tensor information, the thermal history is useful to discuss the detailed spatial–temporal deformational kinematic process.

3.3. *Analysis*. In general, the field observations indicate that the structures can be divided into three domains: one has a salient shape (domain I) in the western region, the second has a recessed shape (domain II) in the eastern region, and the third (domain III) is bounded by the North Huicheng Basin strike-slip fault system. This regionalized structural domain is consistent with the individual plate-like movement from the Global Positioning System (GPS) velocities and crustal uniform strain rate fields [51]. The plate-like movement of the West and East Qinling Orogens induced multiple left-lateral strike-slip motions in domain III and controlled the associated structures in domains I and II. This interpretation can well explain the coeval development of the North Huicheng Basin strike-slip fault system and alongside salient and recessed structures. In particular, we focus on how strike-slipping controls salient
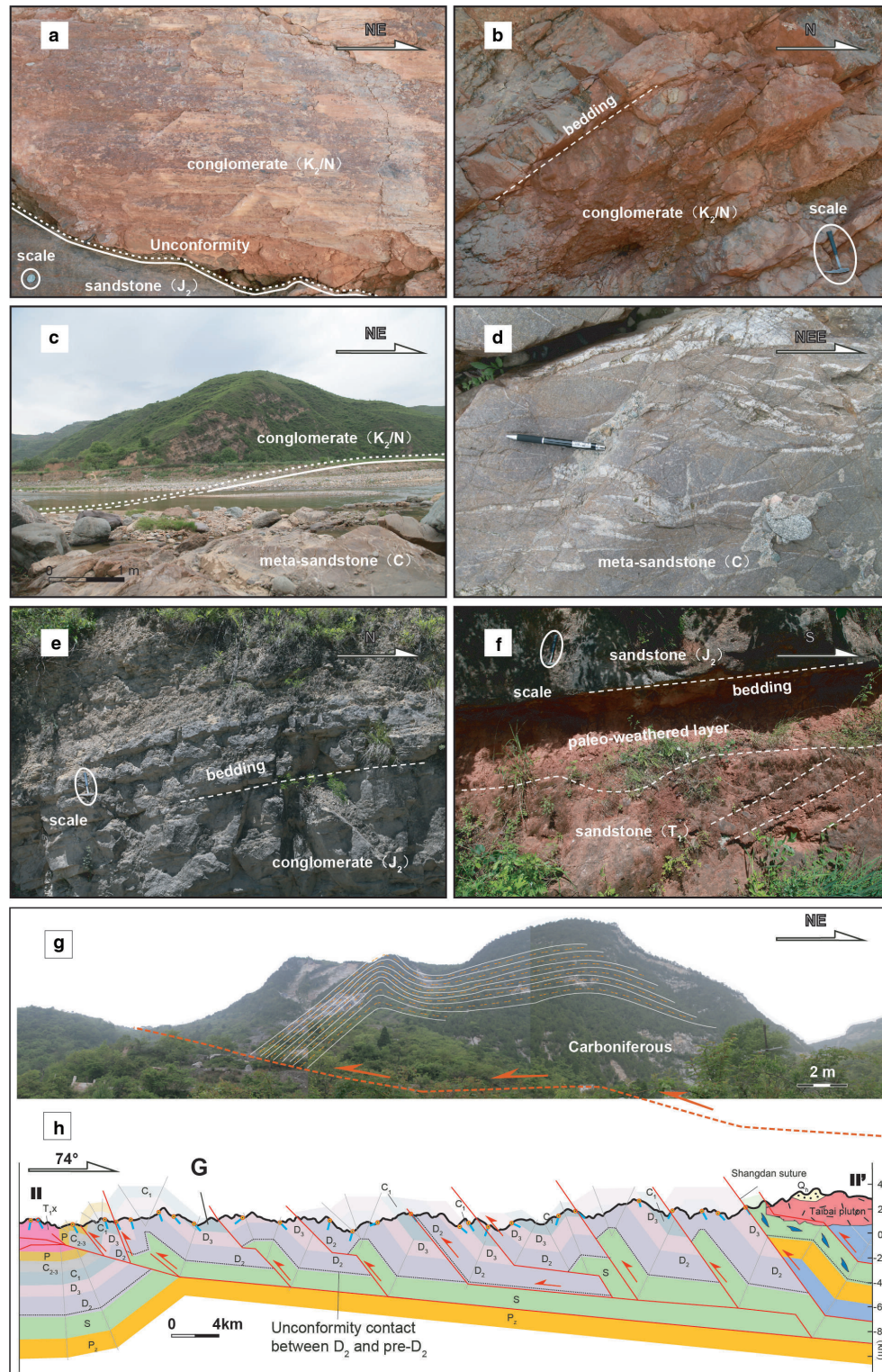
FIGURE 5: Representative photographs illustrating the Jurassic and Cretaceous layer characteristics. (a–c) Terrestrial Cretaceous (K$_1$) conglomerate, sandstone, and other clastic rocks unconformably cover the older strata. (d) Carboniferous meta-sandstone. (e) Middle Jurassic Longjiagou Formation (J$_2$) lacustrine sandstone, shale, and interlayered coal. (f) The unconformable contact between the Longjiagou Formation (J$_2$) and the Lower Triassic Renjiagou Formation (T$_1$). (g) The fault-related fold on the east side of the North Huicheng Basin strike-slip fault, which indicates southwestward thrusting. (h) Cross-section II-II' modified from Reference 36; the location is shown in Figure 2(b).

TABLE 1: Field paleostress tensor data.

Data set	Location	Lithology	Age	Fracture		Slip line		Slip sense	σ_1	σ_2	σ_3
				Dip direction (°)	Dip (°)	Pitch (°)	Trend				
1	N33°53′37.9″	Metasiltstone	S/D	350	60	13	E	L	23/229	62/011	16/132
	E105°41′19.8″			009	50	25	W	L			
				354	70	15	E	L			
				352	60	19	E	L			
				357	51	20	E	L			
				353	66	15	W	L			
				012	67	30	W	L			
				015	75	25	W	L			
				010	80	22	W	L			
				017	60	15	W	L			
2	N 33°51′35.3″	Sandstone	J$_2$	320	75	60	W	N	67/106	15/235	12/325
	E 105°42′23.7″			305	70	68	E	N			
				311	70	71	E	N			
				313	68	75	E	N			
				337	51	74	E	N			
				343	66	59	E	N			
				312	67	65	E	N			
				295	75	25	E	N			
				286	80	22	E	N			
				335	60	76	E	N			
3	N 33°55′57.4″	Metasiltstone	D	355	63	23	E	L	02/215	64/310	26/124
	E 106°04′58.8″			358	70	26	E	L			
				350	63	15	E	L			
				349	60	29	E	L			
				357	51	20	E	L			
				353	66	15	W	L			
				165	76	22	W	L			
				348	75	25	W	L			
				160	70	32	E	L			
				355	72	28	E	L			
4	N 33°53′58.0″	Sandstone	K$_1$	009	50	75	E	I	09/162	19/255	69/047
	E 106°18′31.9″			167	70	52	E	I			
				162	63	68	E	I			
				175	65	72	E	I			
				165	69	74	E	N			
				172	66	78	E	I			
				165	76	74	W	I			
				359	81	73	W	N			
				162	72	75	E	I			
				173	72	68	E	I			

(*Continued*)

TABLE 1: Continued

Data set	Location	Lithology	Age	Fracture		Slip line		Slip sense	σ_1	σ_2	σ_3
				Dip direction (°)	Dip (°)	Pitch (°)	Trend				
5-old	N 33°44′46.3″	Sandstone	K_1	343	64	69	W	I	04/335	06/066	83/209
	E 105°47′35.1″										
				330	70	74	W	I			
				346	63	68	W	I			
				350	72	72	W	I			
				165	65	74	E	R			
				172	64	78	E	I			
5-young	N 33°44′46.3″	Sandstone	K_1	326	80	59	W	N	56/165	17/047	28/308
	E 105°47′35.1″										
				305	75	63	W	N			
				335	69	71	W	N			
				150	63	75	W	I			
				320	71	72	E	N			
				325	75	59	W	N			
				311	72	68	E	N			
				324	74	60	W	N			
6	N 33°47′46.8″	Sandstone	K_1	356	65	80	W	I	16/348	11/081	70/203
	E 106°00′10.9″										
				358	67	79	W	I			
				005	68	68	W	I			
				170	83	78	E	I			
				172	78	75	E	I			
				003	71	75	W	I			
				350	69	72	W	I			
				359	71	74	W	I			
				349	68	73	W	I			

Note: The numerical dynamic analysis method P-B-T axes method (PBT; Turner, 1953) was used for the calculation of principal stress directions ($\sigma_1 \geq \sigma_2 \geq \sigma_3$). For σ_1 to σ_3, azimuth (first number) and plunge (second number) of the principal stress axes are given. S/D—Silurian/Devonian; J_2—Middle Jurassic; K_1—Middle Cretaceous; E—East; W—West; K—Cretaceous; L—Left strike-slip fault; N—Normal fault; I—Inverse fault.

and recessed structures in one or two shortening directions, which is the key controversial issue in this study. The southwestward thrust fault (Figure 5(g)) in the east side recessed fold-and-thrust belt indicates a consistent shortening direction with that of the salient structures (Figure 3(b)). This evidence is consistent with published cross-sections (Figure 4(b), cross-section I-I′; Figure 5(h), cross-section II-II′) [36]. In this way, the one-direction shortening model (Figure 3(b)) is most favored based on field observations. Furthermore, the paleostress tensor data indicate that it underwent multiple left-lateral strike-slip faulting and complex tectonic events in this region (Figure 2(b)).

4. Analog Modeling

4.1. Set-Up of the Analog Experiment. Sandbox modeling has been widely used to investigate continental deformation

[52–59], such as strike-slip faults and associated structures [60–62]. Inspired by the published sandbox models, the analog model here is set up as one direction shortening, with one fixed lateral vertical glass wall and one free boundary (Figure 7). Plates A and B are used to illustrate the West and East Qinling deformation domains, respectively. Plate A is pushed through a mobile backstop to shorten the model (Figure 7(a)). With a transfer force through the plate border, plate B was passively pushed forward, while plate A was moving (Figure 7(a)). The experimental velocity can be illustrated by the following equation:

$$V_b^e = \mu V_a (\cos(\alpha))^2 = \mu V (\cos(\alpha))^2$$

where V_b^e is the efficient velocity parallel to the shortening direction in plate B, μ is the correlation coefficient, V_a is the efficient velocity parallel to the
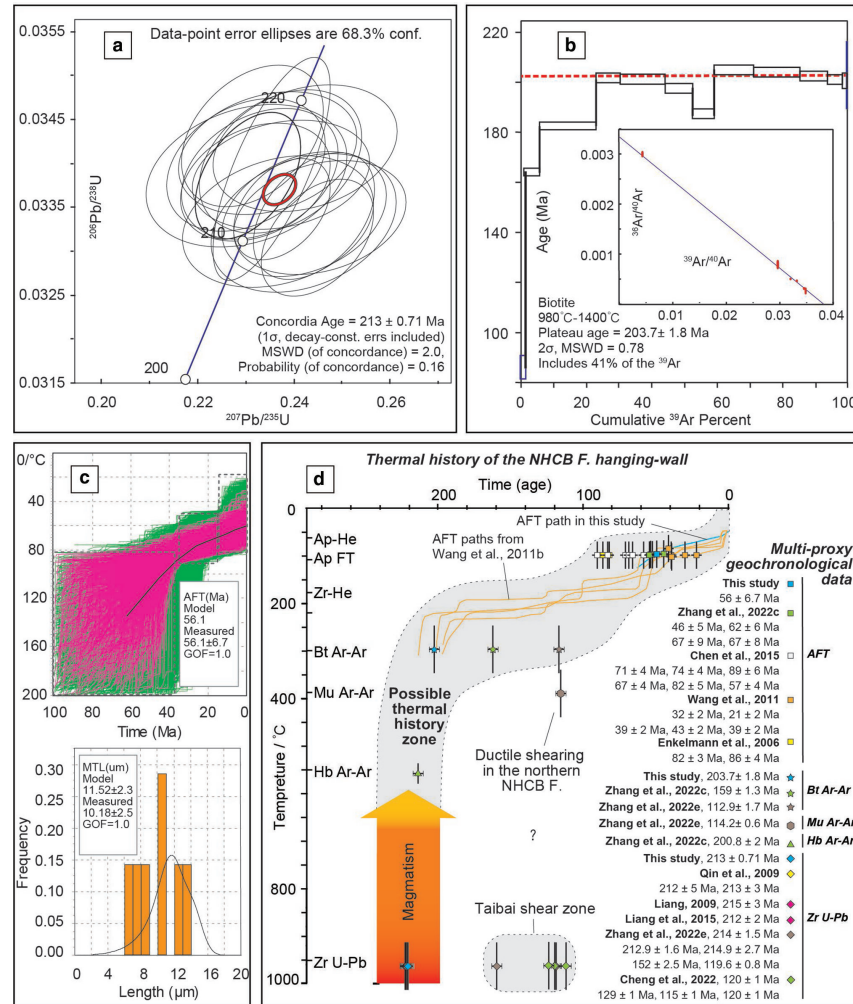
FIGURE 6: Multiproxy geochronological dating results from a granodiorite in the hanging wall of the North Huicheng Basin Fault. (A) Concordant zircon U-Pb ages. (B) Biotite ^{40}Ar/^{39}Ar ages. (C) Apatite fission-track age data. (D) Temperature-time path from our and published thermochronological ages (data from this study and References 22, 28, 36, 38, 39, 86, 87). Zr—zircon; Hb—hornblende; Mu—muscovite; Bt—biotite; Ap—apatite.

shortening direction on plate A, V is the shortening velocity with respect to the mobile backstop (Figure 7), and α is the plate border angle. Since gravity is equal for both the prototype and model and the densities have the same order of magnitude, the concept of dynamic similarity implies that the ratio of stresses is nearly equal to the ratio of lengths [63, 64]. The used sand has an angle of internal friction of ca. 42°, a density of ca. 1560 kg/m^{-3}, and negligible cohesion. The ratio was chosen to be 1.5×10^{-6} (Table 5).

4.2. Results. The analog experiments were performed in the Tectonophysics Experiment Platform of the Laboratory of Deep Earth Science and Exploration Technology, Ministry of Natural Resources, China. During the shortening, we collect images of the experiment at 5 seconds intervals with a Canon 80D camera. Then, we recorded and calculated the displacement and rotation fields via PIV (Figure 8 and -continued). In map view, the displacement was usually accommodated by thrust

sheets, which developed in a forward direction, and the distance was evenly distributed (figures 8 and 9). The frontier displacement field obtained from particle image velocimetry in the plate A domain was parallel to the shortening direction (Figure 8). However, the particles displayed counterclockwise motion in the transition zone and perpendicular motion to the shortening direction on plate B (Figure 8 and -continued). In a cross-sectional view, the sand layers were thickened around a frontal fault ramp. When a thrust sheet migrated forward, the shortening was accommodated by a new thrust at the front of the mobile sand layer (Figure 9(c) and 9(d)). The thrust sheets in plate A (cross-section a-a') occurred more frequently, and the thrust sheet distance was larger than that in plate B (cross-section b–b'; Figure 9(e) and 9(f)). The highest point of each thrust sheet grew gradually under continuous shortening (Figure 9(e) and 9(f)). The topographic slope was ~32° in the cross-section a–a' forelimb, while it was ~30° in the cross-section b–b' forelimb (Figure 9(c) and 9(d)).

Table 2: Zircon U-Pb geochronologic analyses by LA-ICP-MS spectrometry.

| Analysis spots | Isotopic ratios | | | | | | Isotopic age (Ma) | | | | | | | Concordance |
	$^{207}Pb/^{206}Pb$	1σ	$^{207}Pb/^{235}U$	1σ	$^{206}Pb/^{238}U$	1σ	$^{207}Pb/^{206}Pb$	1σ	$^{207}Pb/^{235}U$	1σ	$^{206}Pb/^{238}U$	1σ	Th/U	(%)
YP150603-8(1)														
P01	0.05	0.00	0.24	0.01	0.03	0.01	287.10	85.17	214.97	6.58	215.20	5.23	1.18	99%
P02	0.05	0.00	0.23	0.01	0.03	0.01	172.31	64.80	210.79	5.95	214.71	2.97	0.73	98%
P03	0.05	0.00	0.25	0.01	0.03	0.01	366.72	66.66	222.69	6.28	210.32	2.75	0.53	94%
P04	0.05	0.00	0.24	0.01	0.03	0.01	366.72	75.92	222.10	6.77	211.85	2.97	0.81	95%
P05	0.05	0.00	0.23	0.01	0.03	0.01	153.79	99.06	211.66	8.03	217.51	3.32	0.62	97%
P06	0.05	0.00	0.23	0.01	0.03	0.01	220.44	119.43	214.24	10.03	216.30	2.88	0.65	99%
P07	0.97	0.00	0.00	0.00	0.00	0.00	error	error	0.00	0.00	0.00	0.00	Error	Error
P08	0.05	0.00	0.23	0.01	0.03	0.01	194.53	97.21	212.11	8.41	214.26	2.74	0.74	98%
P09	0.05	0.00	0.23	0.01	0.03	0.01	194.53	136.09	210.61	11.39	214.71	3.33	0.68	98%
P10	0.05	0.00	0.24	0.01	0.03	0.01	227.85	108.32	216.50	9.98	214.78	2.55	0.81	99%
P11	0.05	0.00	0.25	0.01	0.03	0.01	350.06	105.55	223.13	9.61	211.73	2.68	0.66	94%
P12	0.05	0.00	0.24	0.01	0.03	0.01	331.54	107.40	220.40	9.22	212.01	2.93	0.70	96%
P13	0.05	0.00	0.24	0.01	0.03	0.01	261.18	54.62	216.68	5.39	212.32	2.38	1.45	97%
P14	0.05	0.00	0.24	0.01	0.03	0.01	264.88	123.13	220.56	10.31	216.66	2.96	0.85	98%
P15	0.05	0.00	0.23	0.01	0.03	0.01	153.79	107.39	210.46	8.97	215.48	3.12	0.69	97%
P16	0.05	0.00	0.24	0.01	0.03	0.01	324.13	112.02	220.28	10.35	211.36	3.25	0.70	95%
P17	0.05	0.00	0.24	0.01	0.03	0.01	300.06	133.32	216.01	10.73	211.46	3.08	0.74	97%
P18	0.06	0.00	0.23	0.02	0.03	0.01	500.04	146.28	213.64	13.11	189.34	3.92	0.65	87%
P19	0.05	0.00	0.24	0.01	0.03	0.01	238.96	109.25	216.43	9.09	215.73	3.35	0.73	99%
P20	0.05	0.00	0.23	0.01	0.03	0.01	194.53	107.39	212.86	8.81	214.86	3.08	0.83	99%

Table 3: $^{40}Ar/^{39}Ar$ result.

Step	$T(°C)$	$(^{40}Ar/^{39}Ar)_m$	$(^{36}Ar/^{39}Ar)_m$	$(^{37}Ar/^{39}Ar)_m$	$(^{38}Ar/^{39}Ar)_m$	^{40}Ar (%)	F	^{39}Ar ($\times10^{-14}$ mol)	^{39}Ar (Cum.) (%)	Age (Ma)	$\pm1\sigma$ (Ma)
			Sample: YP150603-8 (1), granodiorite, biotite, W = 13.02 mg, J = 0.004549								
1	700	249.7595	0.8082	0.1727	0.1733	4.38	10.9368	0.17	0.95	87.6	4.6
2	770	61.4645	0.1365	0.0000	0.0391	34.36	21.1207	0.90	5.94	165.5	1.6
3	810	29.1815	0.0187	0.0201	0.0176	81.03	23.6467	3.12	23.21	184.3	1.8
4	840	30.1413	0.0132	0.0166	0.0153	87.01	26.2260	1.30	30.38	203.3	1.9
5	870	30.0994	0.0135	0.0035	0.0158	86.77	26.1166	2.49	44.14	202.5	1.9
6	900	29.6522	0.0137	0.0196	0.0159	86.35	25.6056	1.56	52.68	198.8	1.9
7	940	29.6687	0.0184	0.0000	0.0168	81.64	24.2226	1.15	59.03	188.6	1.8
8	980	31.2805	0.0159	0.0730	0.0161	84.94	26.5713	2.20	71.18	205.9	2.0
9	1010	28.7658	0.0078	0.0170	0.0142	92.01	26.4665	2.54	85.20	205.1	1.9
10	1040	29.0032	0.0092	0.0100	0.0151	90.57	26.2686	1.54	93.69	203.6	1.9
11	1080	30.1689	0.0142	0.0350	0.0162	86.08	25.9700	0.82	98.24	201.4	1.9
12	1150	33.8448	0.0268	0.2225	0.0083	76.63	25.9407	0.28	99.77	201.2	3.0
13	1400	231.0399	0.6926	0.7420	0.1377	11.44	26.4374	0.04	100.00	204	13
			Total age = 150.7 Ma. $F = {}^{40}Ar^*/^{39}Ar$, is the ratio of radiogenic Argon[40] and Argon[39]								

TABLE 4: Apatite fission-track results.

			No. of	ρ_d (10^5/cm^2)	ρ_s (10^5/cm^2)	ρ_i (10^5/cm^2)	$P(\chi^2)$	Age (Ma)	MTL (μm±1σ)	
Sample	Location	Lithology	Grains	(N$_d$)	(Ns)	(Ni)	%	(±1σ)	(Nj)	Dpar
YP150603-8(1)	N 33°53′20.70″ E 105°43′25.10″ 1263 m	Granodiorite	35	3.889 (671)	9.837 (1697)	6.955 (6313)	95.7	56 ± 4	11.3 ± 2.4 (97)	1.59

Note: Standard track densities (ρ_d) and induced track densities (ρ_i) were measured on mica external detectors and fossil track densities (ρ_s) on internal mica surfaces. N$_d$, N$_s$, and N$_i$ are the numbers of tracks counted. Ages were calculated using a zeta of 389.4 ± 19.2 (DXB) using Corning CN5 dosimeter glass. If $P(\chi^2) > 5\%$, the single grain ages are contained in the same age group, and the pooled age was used as the age estimate of the sample; whereas if $P(\chi^2) < 5\%$, the central age (the weighted mean age) was used (Galbraith, 1990). Detailed Apatite fission track grain ages, confined fission-track lengths, and Dpar seen in online supplementary Tables S1 and S2.
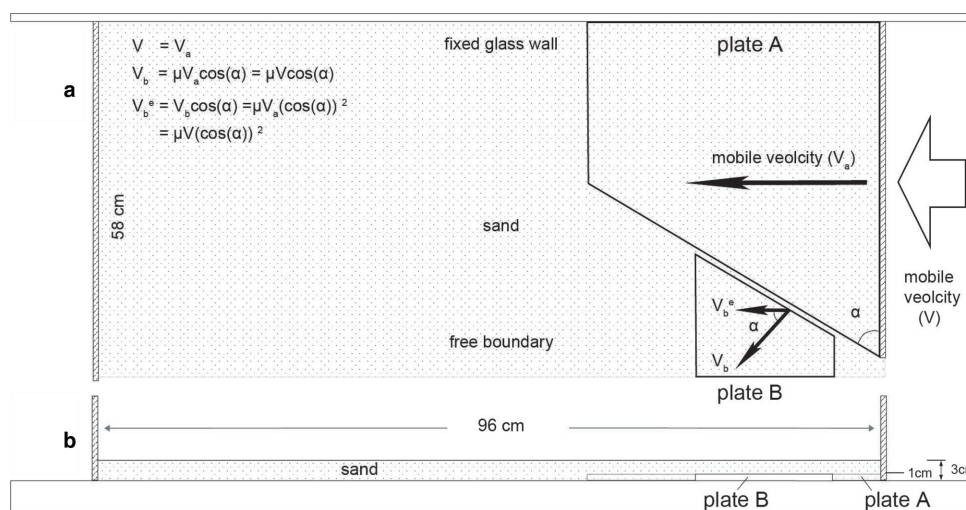
FIGURE 7: The analog model consists of a rigid table with one fixed lateral vertical glass wall, one free boundary, a flat horizontal base, and two plates A and B. With a transfer force through a border, plate B is passively pushed forward, while plate A is moving. Possible velocity relationship between plates A and B. V is the shortening velocity with respect to the mobile backstop, V$_a$ is the efficient velocity parallel to the shortening direction in plate A, V$_b$ is the velocity in plate B, V$_b^e$ is the efficient velocity parallel to the shortening direction in plate B, μ is the correlation coefficient, and α is the plate border angle.

TABLE 5: Scaling ratio used in the analog experiments.

	Model	Nature	Model/nature
Thickness	3 (cm)	20 (km)	1.5×10^{-6}
Length	96 (cm)	640 (km)	1.5×10^{-6}
Width	58 (cm)	387 (km)	1.5×10^{-6}
Convergence distance	11 (cm) (chosen)	73 (km)	1.5×10^{-6}
Density	1.56×10^3 (kg/m^3)	2.7×10^3 (kg/m^3)	5.78×10^{-1}

5. Discussion

5.1. Comparison of Experimental Results With Field Observations. When comparing structures, the experimental results and prototype have a high fitness, which can be used to explore how the strike-slip fault controls salient and recessed structures in nature. In the main strike-slip zone (domain II/II'), evidence of a simple shear component is visible, and the axial plane of anticlines changes to a nearly E–W trend (Figure 10), which is confirmed by the particle counterclockwise rotation via PIV mapping in the sandbox experiment (Figure 8 and -continued). In addition, the structures display multiple left-lateral strike-slip motions, which occurred both in the experiment and in the prototype (Figure 10). With the accommodative effect of strike-slip faulting, transtensional faulting can result in some pull-apart basins (Figure 10).
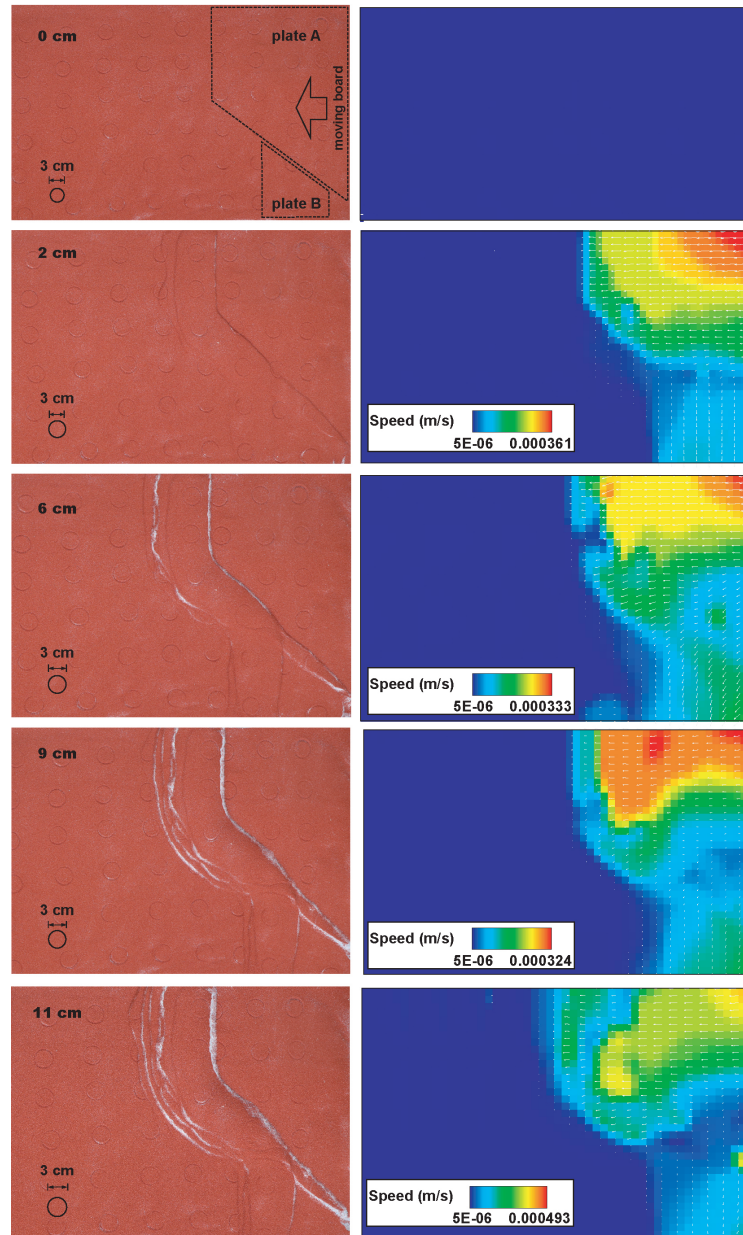
FIGURE 8: Overview of the surface structural development in the experiments with a mobile backstop after 0, 2, and 6 cm of convergence. The right bar is the particle image velocimetry fields and paths, which show the counterclockwise rotation in the transfer zone between the two plates. Overview of the surface structural development in the experiments with a mobile backstop after 9 and 11 cm of convergence.

Domain I (Figure 10(a)) is controlled directly by the motion of plate A, which is very similar to the shape of the salient fold and thrust belts distributed in domain I' (Figure 10(b)). Both in the experiment and prototype, the thrust faults are distributed at approximately equidistant distances, and some coeval fault-related folds also developed (Figure 10). The passive markers (circles with a diameter of 3 cm, Figure 8) in this domain are compressed parallel to the shortening direction and show that the deformation in domain I is pure shear. The salient

thrusts and folds gradually terminate along the North Huicheng Basin strike-slip fault system, and their eastern segments display left-lateral strike-slip motion (Figure 10). In domains III and III', the thrusts and folds are recessed and curve opposite to the shortening direction. Some of the thrust faults and folds should connect at the beginning and are truncated during the shortening process, which is evidenced by the experimental results (Figure 10).

According to the experimental results, it can be inferred that the highest point of each thrust sheet and topographic
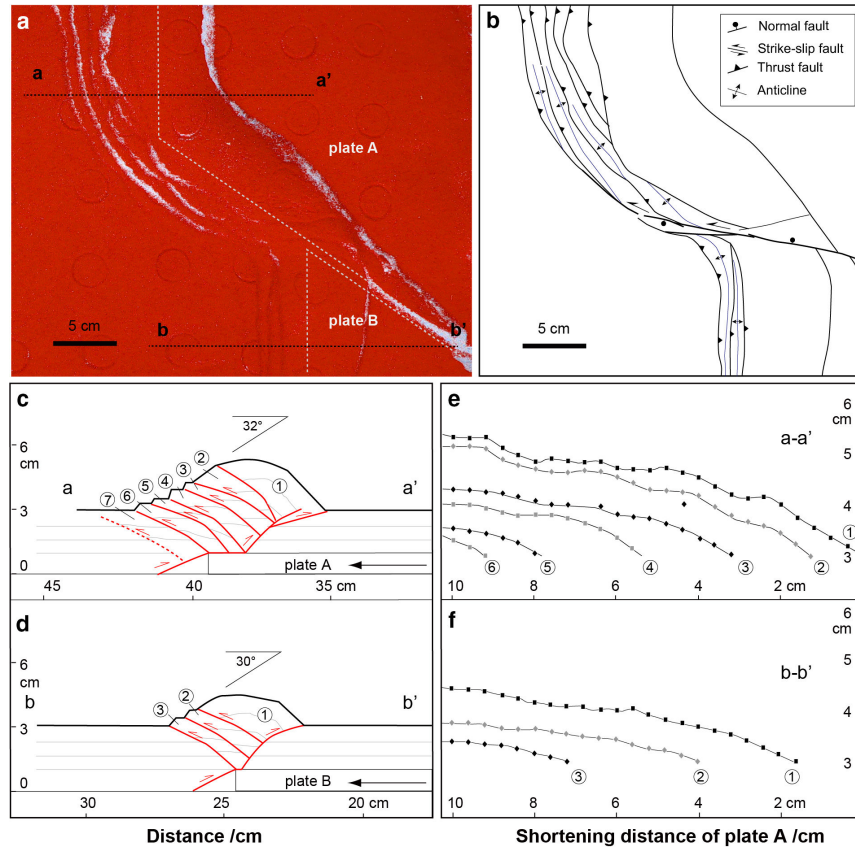
FIGURE 9: Analog modeling results of the 11 cm shortening of plate A. Thrust and fold characteristics in map view (a and b) and cross-section view (c and d). In c and d, the highest point of each sheet grows gradually under the continuous shortening. e and f are the thrust sheet sequences during continuous shortening.
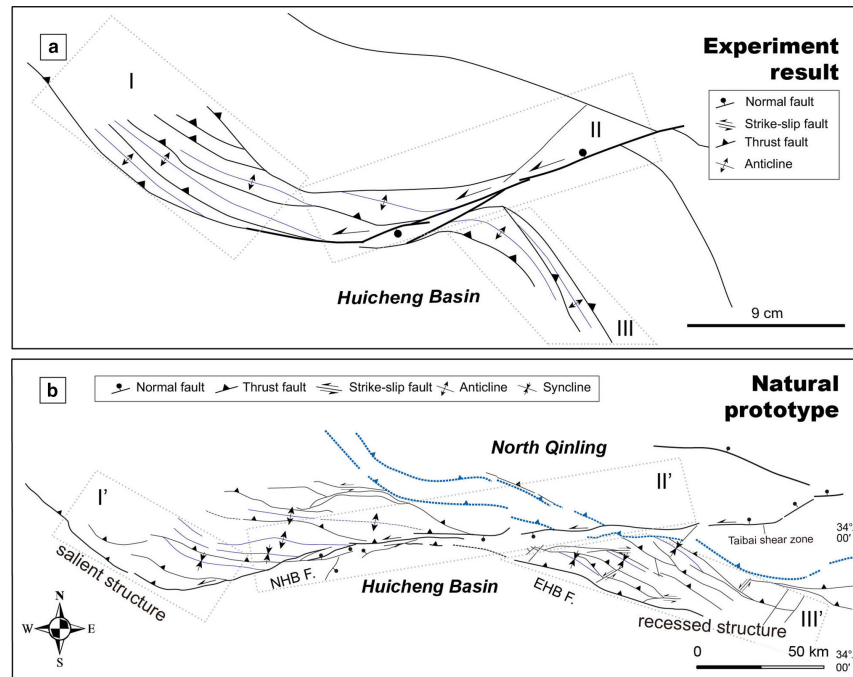

FIGURE 10: Comparison of the analog experiment result (a) with natural protype (b). According to the orientation changes of the thrust faults and associated folds, the sand layers were deformed as two domains I and III, which connect through a strike-slip zone (domain II) during the shortening processes. NHB F.—North Huicheng Basin Fault; EHB F.—East Huicheng Basin Fault.
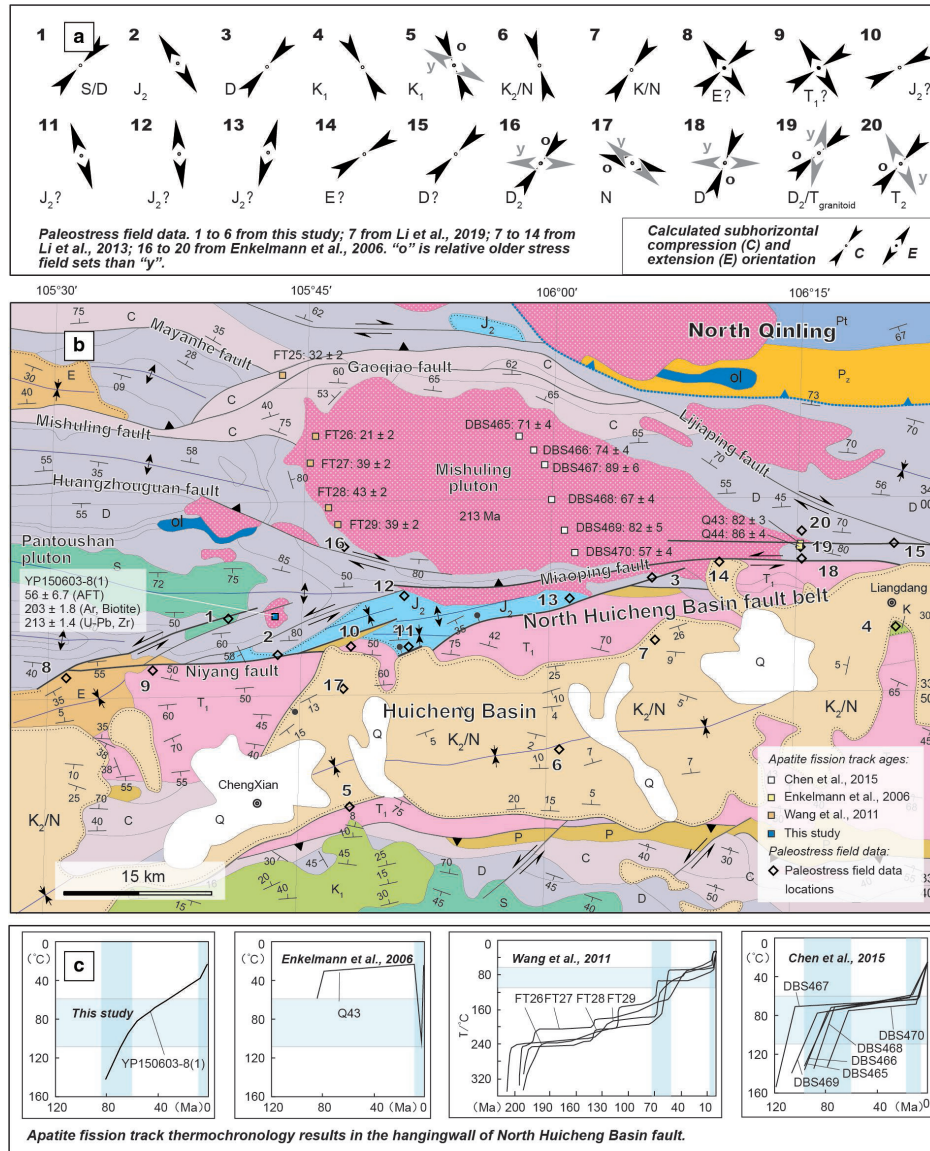
FIGURE 11: Integrated field observation, paleostress, and geochronological data. (a) Paleostress data from this study and Reference 22, 35, 40; arrows around the plots give the calculated local orientations of subhorizontal principal compression and extension. (b) Detailed geologic map of the Huicheng Basin with paleostress and geochronological data location (the legend can be seen in Figure 2). (c) Our and published apatite fission-track model paths, data from this study and References 22, 37, 39.

slope should grow during shortening. Because of the complex weathering and erosion, we can no longer obtain related information in nature. However, in general, the fact that individual plate-like movement induces strike-slipping and controls salient and recessed structures is confirmed by the experimental results (Figure 10).

5.2. Application to the Qinling Orogen. The evidence from geology, geophysics, and geochronology indicates that the Qinling Orogen evolved into intracontinental tectonic processes since the closure of the Paleotethys Ocean [65]. In the Early Triassic, a foreland basin formed in the Huicheng region, which controlled the tectonic setting and resulted in neighboring structures [36, 41]. In the Middle Triassic, the subduction of the Paleotethys oceanic crust

ended the foreland basin in the Huicheng region [41]. In the Late Triassic, widespread syn- to postcollisional plutons were emplaced at 200–230 Ma [31, 38, 66], which is consistent with our zircon U–Pb ages (213 ± 0.7 Ma; Figures 6(a) and 11(b)). Previous analog experiments have confirmed that magma can rise along fault-ramp structures [67–75]. The weak middle crustal zone [36, 76–78] can be activated as a thrust fault ramp [79], such as the ramp in Figure 4(b). This fault-ramp structure might have allowed magma to be emplaced ca. 900°C at 213 Ma (zircon U–Pb [48]; Figures 6(d) and 12(a)). Then, the hanging wall pluton was transported upward to the 300°C ± 50°C isotherm at 203 Ma (biotite ^{40}Ar–^{39}Ar dating [49]).

In the Late Triassic to Jurassic, due to continuous compression from the North and South China Blocks, the
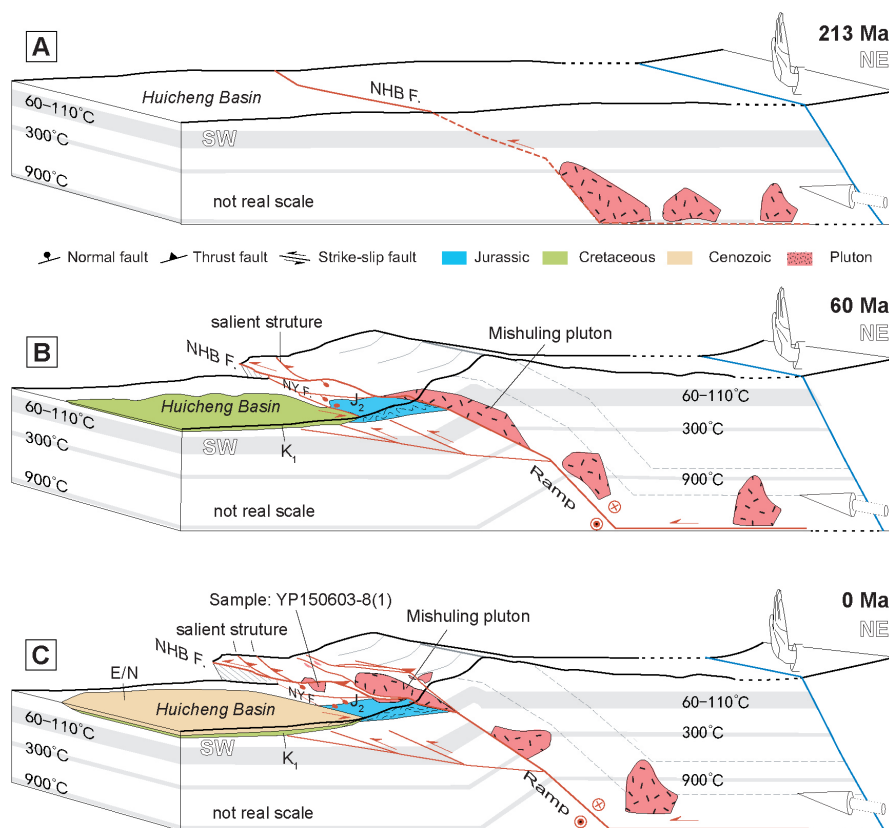
FIGURE 12: Sketch cartoon illustrating the integrated interpretation of the deformation and geothermal history (data from Figure 6(d)) of the North Huicheng Basin deformation belt. Since the late Triassic continental collision, with the multiple strike-slip movements of the fault-ramp structure, the hanging wall rocks have risen to the surface, and pull-apart basins have developed. J_2—Middle Jurassic; K_1—Lower Cretaceous; E/N—Paleogene to Neogene; NHB F.—North Huicheng Basin fault; NY F. —Niyang fault.

Qinling Orogen was mainly characterized by strike-slip faulting and pull-apart basin formation along the major boundary faults [32, 43, 65]. In the North Huicheng strike-slip fault system, the Miaoping fault underwent south-directed thrusting as well as left-lateral strike-slip faulting following the late Triassic collision [28, 80]. Along the Niyang fault, the left-lateral strike-slip faulting transitioned to transtensional faulting and controlled the local development of the half-graben basin during the Middle Jurassic (Figures 11(b) and 12(b)). These strike-slip fault-controlled pull-apart basins are well represented both in our sandbox experiment (Figure 10(a), domain II) and in field observations (Figure 11(a), paleostress sets 2, 9, 10, 11, 12, and 13). Therefore, the Jurassic basin was likely induced by the (1) continuous development of left-lateral strike-slip faulting along the North Huicheng Basin fault system [28], not (2) regional postcollisional collapse [40].

During the Late Jurassic to the Early Cretaceous, the Qinling Orogen underwent an intense intracontinental orogeny, which resulted from the southward intracontinental subduction of the North China Block [65]. The lower Cretaceous Donghe Group is in unconformable contact with the underlying strata in the northern Huicheng Basin (Figure 5(a) and 5(c)), indicating this tectonic event [36]. Meanwhile, large-scale extrusion tectonics [80] developed slightly later or within these

compressional tectonics [40, 78]. The regional escaped tectonics resulted in some strike-slip and associated early Cretaceous basins in the Huicheng region [40], which is supported by our field observations (Figure 11(a), paleostress data 4, 5, and 7). If this is true, the development of left-lateral strike-slip faulting along the North Huicheng Basin fault could have facilitated the development of the pull-apart basin (Figure 12(b)), which can be confirmed by our analog result (Figure 10(a)).

In the Late Cretaceous to Cenozoic, though there are many controversial disputes about the late Mesozoic and Cenozoic basin age [27, 81, 82] and exhumation process [22, 37, 83, 84] in Huicheng region, two tectonic episodes have been reconstructed in most area of the northeastern Tibetan Plateau based on sedimentary geology [27, 29, 35, 85], paleostress data (Figure 11(a), possible paleostress sets 6, 14, and 17) [22, 29, 35, 40], and aAFT data (Figure 11(c)) [22, 36, 37, 39]. In the first episode, long-lasting tectonic quiescence continued with slow exhumation throughout the Late Cretaceous–Paleogene [22, 37] (Figure 11(c)), and the coeval basin was formed. Moreover, the plutons in the hanging wall of the North Huicheng Basin fault remained in the partial annealing zone (PAZ) for a long time (Figures 6(d) and 11(c)), which might be attributable to near-horizontal thrusting along a fault-ramp structure (Figure 12(c)). In the second episode, the late Miocene–early Pliocene

(9, 4 Ma) rapid cooling [22, 37, 39] signifies exhumation from the upper PAZ (90°C and 60°C) to ambient temperatures (Figures 6(d), 11(c) and 12(c)). During these two episodes, the outward growth of the Tibetan Plateau facilitated left-lateral strike-slip and thrusting along the North Huicheng Basin fault system, which predominantly shortened the crust in this region [36].

6. Conclusions

(1) A combination of fieldwork and physical analog modeling outlines the deformation mechanism of the North Huicheng Basin strike-slip fault system and associated structures. The ENE–WSW-trending North Huicheng Basin fault system was induced by the plate-like movement of the West and East Qinling Orogens, which underwent multiple strike-slip faulting and controlled the shape of salient and recessed structures. The scaled physical analog experiment results confirm this hypothesis and reveal the complex spatial–temporal deformational kinematic process of the strike-slip fault system and alongside salient and recessed structures.

(2) Combined with published works, multiproxy geochronological dating (zircon U-Pb age of 213 Ma, biotite ^{40}Ar/^{39}Ar age of 203 Ma, and AFT age of 56 Ma) outlines the main thermal history of the hanging wall of this strike-slip system. Based on the above facts, the integrated research suggests that this multistage strike-slip faulting played a significant role in the main tectonic events, that is, the late Triassic magmatic emplacement, the Jurassic/ Cretaceous local pull-apart basin, and Cenozoic rapid exhumation driven by Tibetan Plateau growth.

Data Availability

The authors declare that all the readers can access the data supporting the conclusions of the study on the Lithosphere website or editor office.

Conflicts of Interest

The authors declare that they have no known competing financial interests or personal relationships that could have appeared to influence the work reported in this paper.

Acknowledgments

Supplementary Materials

The authors declare that all the readers can access the Supplementary Materials on the Lithosphere website or editor office, which are provided as one word and two excel files. Supplementary Materials available: SUPPLEMENTARY MATERIAL 1: Thermochronological analytical methods, Table S1: AFT age and Dpar, Table S2: AFT length data.

References

[1] P. Tapponnier, G. Peltzer, A. Y. Le Dain, R. Armijo, and P. Cobbold, "Propagating extrusion Tectonics in Asia: new insights from simple experiments with Plasticine," *Geology*, vol. 10, no. 12, 1982.

[2] A. Yin and S. Nie, "An Indentation model for the north and South China collision and the development of the Tan-Lu and Honam fault systems, Eastern Asia," *Tectonics*, vol. 12, no. 4, pp. 801–813, 1993.

[3] A. Yin and M. H. Taylor, "Mechanics of V-shaped conjugate strike-slip faults and the corresponding continuum mode of Continental deformation," *Geological Society of America Bulletin*, vol. 123, nos. 9–10, pp. 1798–1821, 2011.

[4] J. Zhang, J. Qu, B. Zhang, et al., "Determination of an Intracontinental transform system along the Southern central Asian Orogenic belt in the latest Paleozoic," *American Journal of Science*, vol. 322, no. 7, pp. 851–897, 2022.

[5] A. V. Zuza and A. Yin, "Continental deformation accommodated by non-rigid passive bookshelf Faulting: an example from the Cenozoic Tectonic development of northern Tibet," *Tectonophysics*, vols. 677–678, no. 10, pp. 227–240, 2016.

[6] A. G. Sylvester, "Strike-slip faults," *Geological Society of America Bulletin*, vol. 100, no. 11, pp. 1666–1703, 1988.

[7] P. England and G. Houseman, "Finite strain calculations of Continental deformation: 2. comparison with the India-Asia collision zone," *Journal of Geophysical Research*, vol. 91, no. B3, pp. 3664–3676, 1986.

[8] A. R. Duvall, M. K. Clark, E. Kirby, et al., "Low-temperature Thermochronometry along the Kunlun and Haiyuan faults, NE Tibetan plateau: evidence for Kinematic change during late-stage Orogenesis," *Tectonics*, vol. 32, no. 5, pp. 1190–1211, 2013.

[9] P. Tapponnier, X. Zhiqin, F. Roger, et al, "Oblique stepwise rise and growth of the Tibet plateau," *Science (New York, N.Y.)*, vol. 294, no. 5547, pp. 1671–1677, 2001.

[10] A. Yin, "Mode of Cenozoic East-West extension in Tibet suggesting a common origin of rifts in Asia during the Indo-Asian collision," *Journal of Geophysical Research*, vol. 105, no. B9, pp. 21745–21759, 2000.

[11] A. M. C. Şengör, C. Zabcı, and B. A. Natal'in, "Continental transform faults: congruence and Incongruence with normal plate Kinematics," *Transform Plate Boundaries and Fracture Zones*, 169–247, 2019.

[12] J. Zhang and D. Cunningham, "Kilometer-scale refolded folds caused by strike-slip reversal and Intraplate shortening in the Beishan region, China," *Tectonics*, vol. 31, no. 3, 2012.

[13] F. Cheng, M. Jolivet, G. Dupont-Nivet, L. Wang, X. Yu, and Z. Guo, "Lateral extrusion along the Altyn Tagh fault, Qilian shan (NE Tibet): insight from a 3d Crustal budget," *Terra Nova*, vol. 27, no. 6, pp. 416–425, 2015.

[14] B. C. Burchfiel, P. Zhang, Y. Wang, et al., "Geology of the Haiyuan fault zone, Ningxia-Hui autonomous region, China, and its relation to the evolution of the Northeast-ern margin of the Tibetan plateau," *Tectonics*, vol. 10, no. 6, pp. 1091–1110, 1991.

[15] A. R. Duvall and M. K. Clark, "Dissipation of fast strike-slip Faulting within and beyond northeastern Tibet," *Geology*, vol. 38, no. 3, pp. 223–226, 2010.

[16] P. England and P. Molnar, "Right-lateral shear and rotation as the explanation for strike-slip Faulting in Eastern Tibet," *Nature*, vol. 344, no. 6262, pp. 140–142, 1990.

[17] X. Chen, A. Yin, G. E. Gehrels, et al., "Two phases of Mesozoic North-South extension in the Eastern Altyn Tagh range, northern Tibetan plateau," *Tectonics*, vol. 22, no. 5, 2003.

[18] Z. Chen, X. Wang, A. yin, B. Chen, and X. Chen, "Cenozoic left-slip motion along the central Altyn Tagh fault as inferred from the sedimentary record," *International Geology Review*, vol. 46, no. 9, pp. 839–856, 2004.

[19] A. Yin, P. E. Rumelhart, R. Butler, et al., "Tectonic history of the Altyn Tagh fault system in northern Tibet inferred from Cenozoic sedimentation," *Geological Society of America Bulletin*, vol. 114, no. 10, pp. 1257–1295, 2002.

[20] M. K. Clark and L. H. Royden, "Topographic ooze: building the Eastern margin of Tibet by lower Crustal flow," *Geology*, vol. 28, no. 8, 2000.

[21] L. Ding, P. Kapp, F. Cai, et al., "Timing and mechanisms of Tibetan plateau uplift," *Nature Reviews Earth & Environment*, vol. 3, no. 10, pp. 652–667, 2022.

[22] E. Enkelmann, L. Ratschbacher, R. Jonckheere, et al., "Cenozoic Exhumation and deformation of northeastern Tibet and the Qinling: is Tibetan lower Crustal flow diverging around the Sichuan Basin?," *Geological Society of America Bulletin*, vol. 118, nos. 5–6, pp. 651–671, 2006.

[23] X. Shen, X. Yuan, and M. Liu, "Is the Asian Lithosphere Underthrusting beneath northeastern Tibetan plateau? insights from seismic receiver functions," *Earth and Planetary Science Letters*, vol. 428, nos. 3–4, pp. 172–180, 2015.

[24] Y. Sun and M. Liu, "Rheological control of lateral growth of the Tibetan plateau: numerical results," *Journal of Geophysical Research*, vol. 123, no. 11, 2018.

[25] C. Wang, J. Dai, X. Zhao, et al., "Outward-growth of the Tibetan plateau during the Cenozoic: a review," *Tectonophysics*, vol. 621, no. 1, pp. 1–43, 2014.

[26] Y. Zhang, S. Dong, and J. Li, "Late Paleogene Sinistral strike-slip system along East Qinling and in Southern North China: implications for interaction between collision-related block Trans-rotation and Subduction-related back-arc extension in East China," *Tectonophysics*, vol. 769, no. 8, p. 228181, 2019.

[27] X. Hu, Y. Zhang, Y. Li, S. Ma, and J. Li, "Post-Orogenic Tectonic evolution of the Qinling belt, central China: insights from a Magnetostratigraphic study of a Cretaceous intra-mountain Basin sedimentary succession," *Journal of Asian Earth Sciences*, vol. 202, p. 104496, 2020.

[28] W. Liang, G. Zhang, Y. Bai, C. Jin, and P. Nantasin, "New insights into the Emplacement mechanism of the late Triassic granite Plutons in the Qinling Orogen: a structural study of the Mishuling Pluton," *Geological Society of America Bulletin*, vol. 127, nos. 11–12, pp. 1583–1603, 2015.

[29] X. Yang, Y. Dong, L. Xiang, et al., "Two phases of Cenozoic deformation in the Wudu Basin, West Qinling (central China): implications for outward expansion of the Tibetan plateau," *Journal of Asian Earth Sciences*, vol. 229, nos. 1–2, p. 105152, 2022.

[30] Y. Dong, X. Shi, S. Sun, et al., "Co-evolution of the Cenozoic Tectonics, Geomorphology, environment and Ecosystem in the Qinling mountains and adjacent areas, central China," *Geosystems and Geoenvironment*, vol. 1, no. 2, p. 100032, 2022.

[31] Y. Dong, G. Zhang, F. Neubauer, X. Liu, J. Genser, and C. Hauzenberger, "Tectonic evolution of the Qinling Orogen, China: review and synthesis," *Journal of Asian Earth Sciences*, vol. 41, no. 3, pp. 213–237, 2011.

[32] L. Ratschbacher, B. R. Hacker, A. Calvert, et al., "Tectonics of the Qinling (central China): Tectonostratigraphy, Geochro-nology, and deformation history," *Tectonophysics*, vol. 366, nos. 1–2, pp. 1–53, 2003.

[33] G. Zhang, B. Zhang, X. Yuan, and Q. Xiao, *Qinling Orogenic Belt and Continental Dynamics*, Science press, 2001.

[34] T. Zhao, G. Zhu, S. Lin, and H. Wang, "Indentation-induced tearing of a subducting continent: evidence from the tan–LU fault zone, East China," *Earth-Science Reviews*, vol. 152, no. 2, pp. 14–36, 2016.

[35] S. Li, Y. Zhang, J. Xiong, C. He, and S. Ma, "Evolution history of Cretaceous to Cenozoic structural Tectonic field in the Huicheng Basin along the the Qinling Tectonic belt," *Acta Geologica Sinica*, vol. 93, no. 8, pp. 1885–1902, 2019.

[36] Y. Zhang, X. Chen, A. V. Zuza, et al., "Testing the Cenozoic lower Crustal flow beneath the Qinling Orogen, northeastern Tibetan plateau," *Journal of Structural Geology*, vol. 165, no. 7, p. 104747, 2022.

[37] H. Chen, J. Hu, G. Wu, W. Shi, Y. Geng, and H. Qu, "Apatite fission-track Thermochronological constraints on the pattern of late Mesozoic–Cenozoic uplift and Exhumation of the Qinling Orogen, central China," *Journal of Asian Earth Sciences*, vol. 114, no. 10, pp. 649–673, 2015.

[38] J. Qin, S. Lai, R. Grapes, C. Diwu, Y. Ju, and Y. Li, "Geochem-ical evidence for origin of Magma mixing for the Triassic Monzonitic granite and its enclaves at Mishuling in the Qinling Orogen (central China)," *Lithos*, vol. 112, nos. 3–4, pp. 259–276, 2009.

[39] X. Wang, M. Zattin, J. Li, et al., "Eocene to Pliocene Exhumation history of the Tianshui-Huicheng region determined by Apatite fission track Thermochronology: implications for evolution of the Northeastern Tibetan

plateau margin," *Journal of Asian Earth Sciences*, vol. 42, nos. 1–2, pp. 97–110, 2011.

[40] W. Li, Y. Dong, A. Guo, et al., "Sedimentary fill history of the Huicheng basin in the West Qinling mountains and associated constraints on Mesozoic Intracontinental Tectonic evolution," *Science China Earth Sciences*, vol. 56, no. 10, pp. 1639–1653, 2013.

[41] Y. Zhang, X. Chen, Z. Shao, et al., "Ocean–continent transition of the Northeastern Paleotethys during the Triassic: constraints from Triassic sedimentary successions across the Qinling Orogen, central China," *Journal of Asian Earth Sciences*, vol. 232, no. 2, p. 105264, 2022.

[42] Y. Dong, Z. Yang, X. Liu, et al., "Neoproterozoic amalgamation of the northern Qinling terrain to the North China Craton: constraints from Geochronology and geochemistry of the Kuanping Ophiolite," *Precambrian Research*, vol. 255, pp. 77–95, 2014.

[43] Y. Dong and M. Santosh, "Tectonic architecture and multiple Orogeny of the Qinling Orogenic belt, central China," *Gondwana Research*, vol. 29, no. 1, pp. 1–40, 2016.

[44] S. Li, S. Zhao, X. Liu, et al., "Closure of the proto-Tethys ocean and early Paleozoic amalgamation of Microcontinental blocks in East Asia," *Earth-Science Reviews*, vol. 186, no. 2, pp. 37–75, 2018.

[45] Q.-R. Meng and G.-W. Zhang, "Geologic framework and Tectonic evolution of the Qinling Orogen, central China," *Tectonophysics*, vol. 323, nos. 3–4, pp. 183–196, 2000.

[46] S.S.I.o.G. Survey, Regional Geology of Shaanxi Province, Geological Publishing House, 2017.

[47] R. Marrett and R. W. Allmendinger, "Kinematic analysis of fault-slip data," *Journal of Structural Geology*, vol. 12, no. 8, pp. 973–986, 1990.

[48] D. J. Cherniak and E. B. Watson, "Pb diffusion in Zircon," *Chemical Geology*, vol. 172, nos. 1–2, pp. 5–24, 2001.

[49] T. M. Harrison, I. Duncan, and I. McDougall, "Diffusion of 40Ar in Biotite: temperature, pressure and compositional effects," *Geochimica et Cosmochimica Acta*, vol. 49, no. 11, pp. 2461–2468, 1985.

[50] A. J. W. Gleadow, "Fission-track dating methods: what are the real alternatives?," *Nuclear Tracks*, vol. 5, nos. 1–2, pp. 3–14, 1981.

[51] M. Hao, Y. Li, Q. Wang, W. Zhuang, and W. Qu, "Present-day Crustal deformation within the Western Qinling mountains and its Kinematic implications," *Surveys in Geophysics*, vol. 42, no. 1, pp. 1–19, 2021.

[52] H. Deng, H. A. Koyi, and N. Froitzheim, "Modeling two sequential coaxial phases of shortening in a foreland thrust belt," *Journal of Structural Geology*, vol. 66, nos. 3–4, pp. 400–415, 2014.

[53] H. Deng, H. A. Koyi, and F. Nilfouroushan, "Superimposed folding and thrusting by two phases of mutually Orthogonal or oblique shortening in analogue models," *Journal of Structural Geology*, vol. 83, no. 7, pp. 28–45, 2016.

[54] M. C. Ritter, T. Santimano, M. Rosenau, K. Leever, and O. Oncken, "Sandbox Rheometry: Co-evolution of stress and strain in Riedel– and critical wedge–experiments," *Tectonophysics*, vol. 722, no. 6, pp. 400–409, 2018.

[55] C. Sun, D. Jia, H. Yin, et al., "Sandbox modeling of evolving thrust Wedges with different preexisting topographic relief: implications for the Longmen shan thrust belt, Eastern

Tibet," *Journal of Geophysical Research*, vol. 121, no. 6, pp. 4591–4614, 2016. https://agupubs.onlinelibrary.wiley.com/toc/21699356/121/6.

[56] C. Sun, Z. Li, W. Zheng, et al., "3d geometry of range front blind ramp and its effects on structural Segmentation of the Southern Longmen shan front, Eastern Tibet," *Journal of Asian Earth Sciences*, vol. 181, no. 2, p. 103911, 2019.

[57] C. Sun, Z. Li, A. V. Zuza, et al., "Controls of Mantle Subduction on Crustal-level architecture of Intraplate Orogens, insights from Sandbox modeling," *Earth and Planetary Science Letters*, vol. 584, nos. 1–4, 2022.

[58] C. Wang, X. Cheng, H. Chen, et al., "The effect of foreland Palaeo-uplift on deformation mechanism in the Wupoer fold-and-thrust belt, NE Pamir: constraints from analogue Modelling," *Journal of Geodynamics*, vol. 100, no. 2, pp. 115–129, 2016.

[59] J. Zhou, F. Xu, C. Wei, G. Li, F. Yu, and H. Tong, "Shortening of analogue models with Contractive Substrata: insights into the origin of purely landward-Vergent thrusting wedge along the Cascadia Subduction zone and the deformation evolution of Himalayan–Tibetan Orogen," *Earth and Planetary Science Letters*, vol. 260, nos. 1–2, pp. 313–327, 2007.

[60] S. Marshak, "Thrust Tectonics and hydrocarbon systems: CH. Salients, recesses, arcs, Oroclines, and Syntaxes; a review of ideas concerning the formation of Mapview curves in fold-thrust belts," *Thrust Tectonics and Hydrocarbon Systems*, vol. 82, pp. 131–156, 2004.

[61] K. Reiter, N. Kukowski, and L. Ratschbacher, "The interaction of two Indenters in analogue experiments and implications for curved fold-and-thrust belts," *Earth and Planetary Science Letters*, vol. 302, nos. 1–2, pp. 132–146, 2011.

[62] J. Macedo and S. Marshak, "Controls on the geometry of fold-thrust belt Salients," *Geological Society of America Bulletin*, vol. 111, no. 12, pp. 1808–1822, 1999.

[63] H. Ramberg, *Gravity, Deformation, and the Earth's Crust: In Theory, Experiments, and Geological Application*, Academic Press, 1981.

[64] R. S. White, R. F. P. Hardman, A. B. Watts, R. B. Whitmarsh, and J. –P. Brun, "Narrow rifts versus wide rifts: inferences for the mechanics of Rifting from laboratory experiments," *Philosophical Transactions of the Royal Society of London. Series A*, vol. 357, no. 1753, pp. 695–712, 1999.

[65] Y. Dong, Z. Yang, X. Liu, et al., "Mesozoic Intracontinental Orogeny in the Qinling mountains, central China," *Gondwana Research*, vol. 30, no. 2, pp. 144–158, 2016.

[66] X. Wang, T. Wang, and C. Zhang, "Neoproterozoic, Paleozoic, and Mesozoic Granitoid Magmatism in the Qinling Orogen, China: constraints on Orogenic process," *Journal of Asian Earth Sciences*, vol. 72, no. 2, pp. 129–151, 2013.

[67] M. Bonini, D. Sokoutis, G. Mulugeta, and E. Katrivanos, "Modelling hanging wall accommodation above rigid thrust ramps," *Journal of Structural Geology*, vol. 22, no. 8, pp. 1165–1179, 2000.

[68] H. A. Koyi and B. Maillot, "Tectonic thickening of hanging-wall units over a ramp," *Journal of Structural Geology*, vol. 29, no. 6, pp. 924–932, 2007.

[69] B. Maillot and H. Koyi, "Thrust dip and thrust refraction in fault-bend folds: analogue models and theoretical predictions," *Journal of Structural Geology*, vol. 28, no. 1, pp. 36–49, 2006.

[70] G. Musumeci, F. Mazzarini, G. Corti, M. Barsella, and D. Montanari, "Magma Emplacement in a thrust ramp Anticline: the Gavorrano granite (northern Apennines, Italy)," *Tectonics*, vol. 24, no. 6, 2005.

[71] F. M. Rosas, J. C. Duarte, P. Almeida, W. P. Schellart, N. Riel, and P. Terrinha, "Analogue Modelling of thrust systems: passive vs. active hanging wall strain accommodation and sharp vs. smooth fault-ramp Geometries," *Journal of Structural Geology*, vol. 99, pp. 45–69, 2017.

[72] F. M. Rosas, J. C. Duarte, W. P. Schellart, R. Tomás, V. Grigorova, and P. Terrinha, "Analogue Modelling of different angle thrust-wrench fault interference in a brittle medium," *Journal of Structural Geology*, vol. 74, no. NB4, pp. 81–104, 2015.

[73] O. Galland, P. R. Cobbold, J. de Bremond d'Ars, and E. Hallot, "Rise and Emplacement of Magma during horizontal shortening of the brittle crust: insights from experimental modeling," *Journal of Geophysical Research*, vol. 112, no. B6, 2007.

[74] F. Martínez, D. Montanari, C. Del Ventisette, M. Bonini, and G. Corti, "Basin inversion and Magma migration and Emplacement: insights from basins of northern Chile," *Journal of Structural Geology*, vol. 114, no. 5, pp. 310–319, 2018.

[75] E. C. Ferré, O. Galland, D. Montanari, and T. J. Kalakay, "Granite Magma migration and Emplacement along thrusts," *International Journal of Earth Sciences*, vol. 101, no. 7, pp. 1673–1688, 2012.

[76] H. Li, R. Gao, X. Huang, et al., "Triassic convergence and Tectonic evolution of the West Qinling Orogen: constraints from reflection-Seismology imaging," *Gondwana Research*, vol. 122, pp. 1–10, 2023.

[77] S. Xue, D. Bai, Y. Chen, et al., "Contrasting Crustal deformation mechanisms in the Longmenshan and West Qinling Orogenic belts, NE Tibet, revealed by Magnetotelluric data," *Journal of Asian Earth Sciences*, vol. 176, no. 8, pp. 120–128, 2019.

[78] Y. Zhang, S. Dong, H. Wang, et al., "Coupled Lithospheric deformation in the Qinling Orogen, central China: insights from seismic reflection and Surface-Wave tomography," *Geophysical Research Letters*, vol. 49, no. 14, 2022.

[79] C. Wang, R. Gao, A. Yin, et al., "A mid-Crustal strain-transfer model for Continental deformation: a new perspective from high-resolution deep seismic-reflection profiling across ne Tibet," *Earth and Planetary Science Letters*, vol. 306, nos. 3–4, pp. 279–288, 2011.

[80] W. Liang, G. Zhang, R. Lu, and P. Nantasin, "Extrusion Tectonics inferred from fabric study of the Guanzizhen Ophiolitic Mélange belt in the West Qinling Orogen, central China," *Journal of Asian Earth Sciences*, vol. 78, no. B1, pp. 345–357, 2013.

[81] Z. Wang, P. Zhang, C. N. Garzione, et al., "Magnetostratigraphy and Depositional history of the Miocene Wushan basin on the ne Tibetan plateau, China: implications for middle Miocene Tectonics of the West Qinling fault zone," *Journal of Asian Earth Sciences*, vol. 44, no. 8, pp. 189–202, 2012.

[82] Y.-P. Zhang, W. Wang, and et al., "Oligocene–Miocene northward growth of the Tibetan plateau: insights from Intermontane basins in the West Qinling belt, NW China," *Geological Society of America Bulletin*, 2023.

[83] M. Wang, Y. Tian, B. Zhou, R. Jiao, and G. Zhang, "Instant far-field effects of Continental collision: an example study in the Qinling Orogen, northeast of the Tibetan plateau," *Tectonophysics*, vol. 833, no. 5946, p. 229334, 2022.

[84] Y.-P. Zhang, W.-J. Zheng, W.-T. Wang, et al., "Rapid Eocene Exhumation of the West Qinling belt: implications for the growth of the Northeastern Tibetan plateau," *Lithosphere*, vol. 2020, no. 1, p. 1, 2020.

[85] Z. Yipeng, Z. Wenjun, Y. Daoyang, W. Weitao, and Z. Peizhen, "Geometrical imagery and Kinematic dissipation of the late Cenozoic active faults in the West Qinling belt: implications for the growth of the Tibetan plateau," *Journal of Geomechanics*, vol. 27, no. 2, pp. 159–177, 2021.

[86] L. Zhang, W. Li, and D. Jiang, "Structural and Geochronological constraints on a late Mesozoic Tectonic transformation in the West Qinling Orogenic belt, China," *Display*, 1–26, 2022.

[87] W. Liang, *Intracontinental Tectonic Evolution of Qinling Orogen since Late Triassic Collision*, Northwest University, 2009.